Tracking the route of molecular oxygen in O-2-tolerant membrane-bound [NiFe] hydrogenase

Jacqueline Kalms, Andrea Schmidt, Stefan Frielingsdorf, Tillmann Utesch, Guillaume Gotthard, David von Stetten, Peter van Der Linden, Antoine Royant, Maria Andrea Mroginski, Philippe Carpentier, et al.

PNAS PLUS

Tracking the route of molecular oxygen in O_2-tolerant membrane-bound [NiFe] hydrogenase

Jacqueline Kalms[a,1], Andrea Schmidt[a,1], Stefan Frielingsdorf[b], Tillmann Utesch[b], Guillaume Gotthard[c], David von Stetten[c,2], Peter van der Linden[c,d], Antoine Royant[c,e], Maria Andrea Mroginski[b], Philippe Carpentier[c,f], Oliver Lenz[b], and Patrick Scheerer[a,3]

[a]Charité - Universitätsmedizin Berlin, corporate member of Freie Universität Berlin, Humboldt-Universität zu Berlin, and Berlin Institute of Health, Institute of Medical Physics and Biophysics, Group Protein X-ray Crystallography and Signal Transduction, D-10117 Berlin, Germany; [b]Institut für Chemie, Technische Universität Berlin, D-10623 Berlin, Germany; [c]European Synchrotron Radiation Facility, F-38043 Grenoble, France; [d]Partnership for Soft Condensed Matter (PSCM), F-38043 Grenoble, France; [e]Univ. Grenoble Alpes, CNRS, CEA, Institut de Biologie Structurale (IBS), F-38000 Grenoble, France; and [f]Univ. Grenoble Alpes, CNRS, CEA, Institut de Biosciences et Biotechnologies de Grenoble (BIG)-Laboratoire Chimie et Biologie des Métaux (LCBM), F-38000 Grenoble, France

Edited by Amy C. Rosenzweig, Northwestern University, Evanston, IL, and approved January 24, 2018 (received for review July 11, 2017)

[NiFe] hydrogenases catalyze the reversible splitting of H_2 into protons and electrons at a deeply buried active site. The catalytic center can be accessed by gas molecules through a hydrophobic tunnel network. While most [NiFe] hydrogenases are inactivated by O_2, a small subgroup, including the membrane-bound [NiFe] hydrogenase (MBH) of *Ralstonia eutropha*, is able to overcome aerobic inactivation by catalytic reduction of O_2 to water. This O_2 tolerance relies on a special [4Fe3S] cluster that is capable of releasing two electrons upon O_2 attack. Here, the O_2 accessibility of the MBH gas tunnel network has been probed experimentally using a "soak-and-freeze" derivatization method, accompanied by protein X-ray crystallography and computational studies. This combined approach revealed several sites of O_2 molecules within a hydrophobic tunnel network leading, via two tunnel entrances, to the catalytic center of MBH. The corresponding site occupancies were related to the O_2 concentrations used for MBH crystal derivatization. The examination of the O_2-derivatized data furthermore uncovered two unexpected structural alterations at the [4Fe3S] cluster, which might be related to the O_2 tolerance of the enzyme.

oxygen-tolerant [NiFe] hydrogenase | metalloproteins | iron–sulfur cluster | X-ray crystallography | crystal derivatization

In many enzymes, the catalytic centers are deeply buried within the protein matrix. In these cases, substrate access and the transport of intermediates and product release are often facilitated by dedicated molecular tunnels (1). A sheltered active site in combination with molecular tunnels can have several advantages for the enzyme: (*i*) an increase of the catalytic efficiency compared with free diffusion, (*ii*) protection of the active site from reactive and inhibitory compounds, (*iii*) protection of unstable intermediates, (*iv*) improved transport time between active sites, (*v*) increased substrate selectivity, and (*vi*) regio- and/or stereospecific control (1, 2). In multifunctional enzymes, molecular tunnels connect the different sites of intermediate generation and utilization. A very well-studied enzyme with multiple active sites is the class I amidotransferase, carbamoyl phosphate synthetase (CPS). The intermediates ammonia and carbamate migrate through a permanent tunnel with a length of almost 100 Å. The CPS structure also revealed a difference in tunnel diameter adjusting to the dimensions of the intermediate (3). The intramolecular tunnel of glutamine phosphoribosylpyrophosphate amidotransferase (GPATase) shows a different architectural feature. GPATase catalyzes the conversion of phosphoribosylpyrophosphate into phosphoribosylamine. Here, the intermediate tunnel between the two active sites only exists temporarily upon binding of the correct ligand to the active site, which further induces consecutive conformational changes of the protein backbone (4). In enzymes like glutamate synthase and glucosamine 6-phosphate synthase, the substrate tunnel is obstructed and switches between an open state and a closed state through substrate-induced conformational changes of amino acids, which act as a gate (5, 6).

In other enzymes, the molecular tunnels connect the protein exterior with the active site deeply buried within the protein matrix. Such tunnels can serve as permanent or gated substrate pathways as found in DhaA haloalkane dehalogenase or cholesterol oxidase, respectively (7, 8). In lipoxygenases, two permanent hydrophobic tunnels that might be used individually by the two substrates, lipid and dioxygen, merge at the active site (9, 10). The nature of gas-substrate tunnels has also been described in various metalloenzymes by using protein structure and gas diffusion kinetics (11, 12). A recent study on the gas tunnel network of the metalloenzyme, O_2-tolerant [NiFe] hydrogenase and its O_2-sensitive counterparts revealed major structural differences in dimension and complexity (13). Furthermore, tunnel

Significance

Tracking the route of substrates, intermediates, and inhibitors in proteins is fundamental in understanding their specific function. However, following the route of gases like molecular oxygen within enzymes has always been challenging. In protein X-ray crystallography, gases can be mimicked using krypton or xenon (with a higher electron count); however, these have a different physical behavior compared to true substrates/inhibitors. In our crystal structure of the O_2-tolerant membrane-bound [NiFe] hydrogenase (MBH) from *Ralstonia eutropha*, we were able to show the direct path of molecular oxygen between the enzyme exterior and the active site with the "soak-and-freeze" derivatization method. This technique might be useful to detect O_2 traveling routes in many other enzymes.

Author contributions: J.K., A.S., P.C., and P.S. designed research; J.K., A.S., S.F., T.U., G.G., D.v.S., P.v.d.L., P.C., and P.S. performed research; S.F., P.v.d.L., A.R., and P.C. contributed new reagents/analytic tools; J.K., A.S., S.F., T.U., M.A.M., O.L., and P.S. analyzed data; J.K., A.S., S.F., T.U., O.L., and P.S. wrote the paper; J.K., A.S., and P.S. performed crystallographic data collection and refinement; J.K., A.S., G.G., and D.v.S. prepared the crystal samples; S.F. prepared the [NiFe] protein sample; T.U. performed and coordinated the molecular dynamics (MD) simulations; P.v.d.L. and P.C. designed the high-pressure freezing system; P.v.d.L., A.R., and P.C. designed the "soak-and-freeze" methodology; P.v.d.L. and P.C. handled the pressure cells; M.A.M. coordinated the MD simulations; O.L. and P.S. coordinated the project; and P.S. designed the idea and the experiments of the project.

The authors declare no conflict of interest.

This article is a PNAS Direct Submission.

Data deposition: The atomic coordinates and structure factors have been deposited in the Protein Data Bank, www.wwpdb.org (PDB ID codes 5MDL, 5MDJ, 5MDK, and 4TTT).

[1]J.K. and A.S. contributed equally to this work.

[2]Present address: European Molecular Biology Laboratory (EMBL), Hamburg Outstation c/o DESY, D-22607 Hamburg, Germany.

[3]To whom correspondence should be addressed. Email: patrick.scheerer@charite.de.

This article contains supporting information online at www.pnas.org/lookup/suppl/doi:10.1073/pnas.1712267115/-/DCSupplemental.

Published online February 20, 2018.

amino acids seem to influence O_2 diffusion rates and tolerance, as shown in several studies of O_2-sensitive and O_2-tolerant hydrogenases (14–17). In the O_2-tolerant membrane-bound [NiFe] hydrogenase (MBH) of *Ralstonia eutropha*, the protein exterior and the [NiFe] active site are connected via two hydrophobic gas tunnels (13, 18) (Fig. 1, dashed black arrow labeled with "O_2 and H_2"). MBH is composed of three subunits. The large subunit harbors the deeply buried active site, where the reversible catalytic reaction $H_2 \rightleftharpoons 2e^- + 2H^+$ takes place. The small subunit contains an electron relay consisting of three [FeS] clusters (Fig. 1, dashed black arrow labeled with "e^-") that transfer the electrons derived from H_2 oxidation at the active site to the third subunit, a membrane-integral cytochrome b_{562}. The cytochrome itself is connected to the quinone pool of the respiratory chain (18, 19). The majority of [NiFe] hydrogenases become inactivated by O_2. MBH is one of few examples that can overcome the O_2 attack by redirecting electrons from the [FeS] clusters back to the [NiFe] active site, where they are used to reduce O_2 completely to harmless water (19–21) (Fig. 1; O_2 and e^-, black dashed arrows). The water molecules are released by a nearby water channel (18) (Fig. 1, dashed blue arrow). Only a small amount of experimental data has been acquired so far exploring the pathways of H_2 and O_2 toward the MBH [NiFe] active site. Experimental determination of O_2 migration pathways in proteins by X-ray crystallography has always been challenging due to the weak interaction of O_2 with the amino acids, the high mobility of the gas, and the low electron count. Thus, O_2 pathways were mainly proposed by either computational studies or by using mimicking noble gas molecules such as krypton or xenon (13, 22, 23).

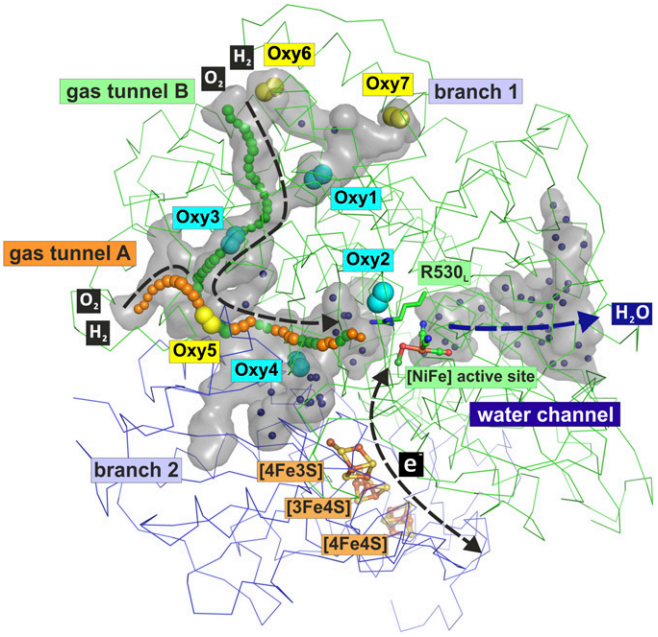

Fig. 1. Overview of substrate and product flow. A C-alpha representation of the large (green) and small (blue) subunits of O_2-derivatized MBH (PDB ID code 5MDL) is illustrated. The [NiFe] active site and the three [FeS] clusters are depicted in ball/stick representation. The hydrophobic gas tunnel and the hydrophilic water channel are shown as gray surfaces calculated with PyMOL (29). Molecular oxygen and water molecules are shown as spheres in cyan/yellow and blue, respectively. Amino acid $R530_L$, which was used as the initial starting point for the CAVER 3.0 tunnel calculation (25), is shown in stick representation. The CAVER results are pictured as orange and green chains of spheres with bottleneck radii of 1.4 Å and 1.3 Å, respectively. Branches 1 and 2 are cavities with no CAVER 3.0-calculated opening toward the protein surface. The directions of the flow of H_2/O_2 molecules, electrons, and water molecules are illustrated as black and blue dashed arrows.

Here, we present the crystal structure of MBH prepared by a "soak-and-freeze" derivatization method that reveals defined O_2 sites in two hydrophobic tunnels leading to the active site and a "dead-end" cavity. These observations are in good agreement with molecular dynamics (MD) simulations suggesting an O_2 "hopping" process through these tunnels.

Results and Discussion

In our protein crystallography experiments, we applied the soak-and-freeze method, recently established at the European Synchrotron Radiation Facility (ESRF) (24), to investigate whether O_2 reaches the [NiFe] active site through a dedicated hydrophobic tunnel network. This technique differs fundamentally from previous crystal derivatization methods as the crystals are flash-frozen in the corresponding gas in its liquid form while still under pressure. This facilitates crystal derivatization at high pressure using difficult-to-handle, highly mobile gases like krypton and molecular oxygen. The specially designed sample supports allow for higher throughput and direct use at synchrotron beamlines. MBH crystals were grown and subsequently exposed to molecular oxygen in a gas pressure cell at 56 bar and 70 bar, which is equivalent to dissolved O_2 concentrations of 72.8 mM and 91 mM, respectively. After incubation for time periods ranging from 15 to 70 min, the derivatized crystals were flash-frozen in liquefied O_2 at 77 K (Table 1). Subsequently, the gas pressure cell was depressurized and the crystals were transferred to liquid nitrogen (LN2) for analysis at the synchrotron beamline. For all O_2-derivatized crystals, a nonderivatized reference (REF) dataset was collected using MBH crystals from the same crystallization batch (Table 2). The O_2 positions were determined by examining the $Fo^{O_2} - Fo^{\text{reference}}$ electron density map calculated using structure factors of the O_2-derivatized (OxD) and REF datasets (Fig. 2 and Fig. S1, including additional final 2mFo − DFc, Fo − Fc difference and simulated-annealing omit electron density maps for all four O_2 molecules). The dioxygen positions were discriminated from water molecules by (*i*) their residence in hydrophobic tunnel cavities (Table 3), (*ii*) comparison with the REF dataset showing no difference in electron density at the same positions, (*iii*) inspection of geometry and distances to surrounding amino acids and (*iv*) correlation with the krypton sites of Kr-derivatized MBH (Fig. S2). Using the soak-and-freeze technique, we identified seven O_2 locations (Oxy1–7) in the best dataset (Fig. 1), which were located within the hydrophobic gas tunnel network. Oxy1–4 were modeled into the protein structure because of an occupancy of at least 50%. The real-space correlation coefficients for all four are above 91% (Table 3). Three of the O_2 molecules (Oxy5–7) showed occupancies of less than 40%, and were therefore not modeled in the structure [Protein Data Bank (PDB) ID code 5MDL]. The majority of the O_2 sites found in the structure describe a continuous pathway between the protein exterior and the [NiFe] active site. One O_2 molecule (Oxy2) resides in a hydrophobic pocket surrounded by amino acids $M30_L$, $V46_L$, $S47_L$, $F569_L$, $E570_L$, $L573_L$, and $L591_L$ (subscript indicates subunit: L, large subunit; S , small subunit) (Figs. 1 and 2 and Table 3). Owing to the 2D representation of Figs. 1 and 2, Oxy2 appears to be close to the [NiFe] active site, but the actual distance is 16.3 Å. A maximum occupancy of 100% was observed for Oxy1 at 70 bar after 15 min of soaking in pressurized O_2 before freezing. Using Oxy1 as a benchmark, we can clearly deduce a correlation of O_2 occupancy with pressure and incubation time (Table 1). To inspect the positions of the O_2 molecules with respect to the gas tunnel network, the latter was calculated with the program CAVER 3.0 (25), using the highly conserved residue $R530_L$ as the initial starting point (Fig. 1). The program predicts two subunit-crossing tunnels, which merge before reaching the [NiFe] active site. Tunnel A, with a minimal diameter (d_{min})

Table 1. Characteristics of O_2 derivatization experiments

Dataset	Pressure, bar	Time, min	Resolution, Å	Occupancy Oxy1, %	Fe4-E76$_s$ distance, Å	OH^- ligand, %
1	56	15	1.35	63	2.8	31
2	56	15	1.30	72	2.8	27
3	56	15	1.42	71	3.1	36
4	56	15	1.44	80	2.8	28
6	56	30	1.31	79	2.5	22
7	56	30	1.45	73	2.8	39
8	56	30	1.27	92	2.4	35
9	56	30	1.32	91	2.5	41
10	56	60	1.55	91	2.6	38
5	56	77	1.37	62	2.9	36
11	70	15	1.41	100	2.6	45
12	70	15	1.45	91	2.7	32

of ∼1.4 Å and a length of ∼33 Å, is categorized as the primary gas tunnel, whereas tunnel B (d_{min} of ∼1.3 Å and length of ∼52 Å) may serve as a secondary pathway. Approximately 56% of the amino acids forming the tunnel surface are of hydrophobic character (Fig. S3). The hydrophobic tunnel entrances presumably facilitate access of the gaseous substrates. The highest occupied O_2 site (Oxy1), located in branch 1, has no obvious connection to the protein exterior and might serve as a substrate storage cavity. A similar storage cavity has been proposed by Montet et al. (26) for the O_2-sensitive hydrogenase from *Desulfovibrio gigas*, assuming that some of the hydrophobic cavities serve as gas reservoirs. They have suggested that the concentration of the gaseous substrate in the enzyme affects the enzyme activity. Comparable conclusions have been drawn from the MD simulation results from [NiFeSe] hydrogenase (27). Baltazar et al. (27) deduce from cavities with trapped H_2 molecules that they either hinder H_2 transport to the active site or promote access by storing gas molecules. Considering the low solubility of H_2 in water, the hydrophobic tunnel system might aid in elevating the H_2 concentration above the surrounding medium level. To further inspect a gas reservoir feature, MD simulations of simultaneous H_2 and O_2 transport in the corresponding ratio through the tunnel network, as well as amino acid exchanges within the proposed tunnel wall, might shed further light on this topic. Oxy3 is located within tunnel B near the bottleneck (smallest tunnel diameter) consisting of the amino acids A127$_L$, V131$_L$, and A202$_L$. Oxy4 is positioned close to the bottleneck of tunnel A and the catalytic center (Figs. 2 and 3). The bottleneck in tunnel A has a distance of <3 Å from the [NiFe] active site and consists of amino acids E27$_L$, R530$_L$, P596$_L$, and C597$_L$.

The observations based on the crystallographic structure were compared with MD simulations of MBH in aqueous solution, as described in further detail in *Materials and Methods*. The resulting 300-ns-long trajectories showing the diffusion of O_2 and H_2 molecules suggested a hopping-like movement of O_2 and H_2 molecules (examples for diffusion pathways of four individual O_2 molecules are shown in Movies S1–S4) through the main tunnels (Figs. 2 and 3 and Figs. S3, S5, and S6). Notably, diffusion outside the tunnel system and no permanent tunnel opening was detected in the simulations, which is in agreement with previous calculations performed on a structurally similar O_2-sensitive "standard" [NiFe] hydrogenase (21). Diffusion of gas molecules through the previously proposed water channel (19) was predicted to be unfavorable compared with the gas diffusion through tunnels A and B. O_2 diffusion (hopping process) through the gas tunnel network resulted in high O_2 densities at the Oxy1 and Oxy3 sites (molecule occupancies of >75%) (Fig. 3), which is in excellent agreement with the results of the soak-and-freeze experiment. Furthermore, O_2 molecules were detected in the vicinity of all other experimentally proposed

Table 2. REF dataset experiments

Dataset	Resolution, Å	Fe4-E76$_s$ distance, Å
1	1.40	3.37
2	1.41	3.30
3	1.38	3.50
4	1.36	3.39
5	1.50	3.43

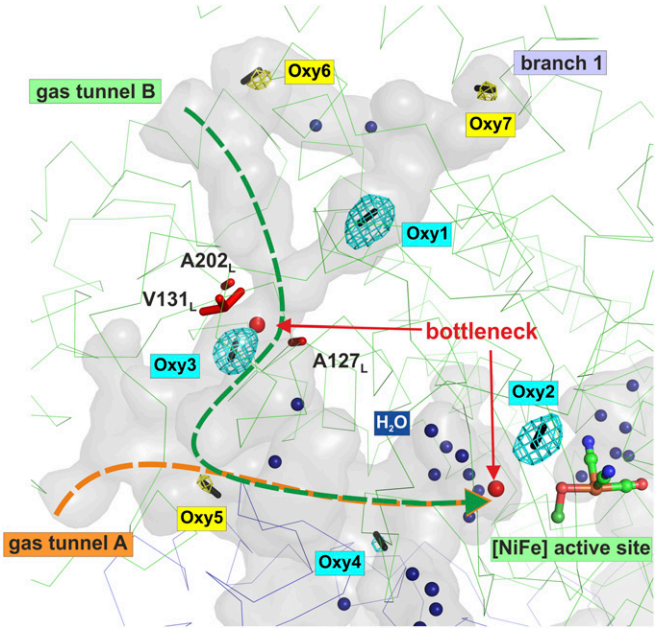

Fig. 2. O_2 locations and the tunnel bottleneck in gas-derivatized MBH. A C-alpha representation of O_2-derivatized MBH (PDB ID code 5MDL) with the hydrophobic gas tunnel shown as a gray surface [calculated with PyMOL (29)] is illustrated. The [NiFe] active site is depicted in ball/stick representation. Oxygen and water molecules are shown as black sticks and blue spheres, respectively. Positions of molecular oxygen are further illustrated as cyan mesh (Oxy1–4) of the $Fo^{O_2} - Fo^{reference}$ electron density map contoured at 3 σ. The Oxy5–7 sites are shown as yellow mesh of the $Fo^{O_2} - Fo^{reference}$ electron density map contoured at 2.5 σ. Gas tunnels A and B, calculated by CAVER 3.0 (25), are pictured as orange and green dashed arrows, respectively. The tunnel A bottleneck is located (red sphere) at the gate to the [NiFe] active site. The bottleneck of tunnel B is composed of amino acids A127$_L$, V131$_L$, and A202$_L$ with the positions marked as red spheres.

Table 3. Characteristics of O_2 molecules in O_2-derivatized MBH

O_2 position	Close environment (distance < 4 Å)	$Fo^{O_2} - Fo^{reference}$ peak [σ (contour level)]	Occupancy, %	Atomic displacement factor of O_2 atoms, Å^2	Real space correlation coefficient
1	$W130_L$, $V280_L$, $I283_L$, $G284_L$, $T473_L$	14.94	100	O1: 29.61 O2: 27.98	0.98
2	$M30_L$, $C32_L$, $V46_L$, $F569_L$, $E570_L$, $L573_L$, $L591_L$	8.41	50	O1: 26.91 O2: 28.21	0.93
3	$A127_L$, $L128_L$, $V131_L$, $A202_L$, $Y206_L$	11.42	62	O1: 29.99 O2: 28.47	0.96
4	$S21_S$, $E22_S$, $I25_S$, $T47_S$	3.69	56	O1: 30.72 O2: 30.92	0.91
5	$K33_S$, $V36_S$, $L37_S$, $L207_L$	<4	<40	O1: 31.35 O2: 26.92	
6	$L150_L$, $I449_L$	<5	<40	O1: 37.63 O2: 34.59	
7	$L438_L$, $S441_L$, $A442_L$, $L462_L$, $L465_L$, $L474_L$	<3	<40	O1: 21.90 O2: 18.34	

locations, as well as within a 3-Å radius from the active site. Due to the side-chain flexibility at room temperature, the positions of the O_2 sites change during the course of the simulations, particularly in tunnel A. This impedes a direct comparison with the experimentally determined values. The assignment of these sites, however, was computationally predicted on the basis of residence times and site occupancies by the O_2 molecules (Fig. 3). Analysis of transition probabilities between the preferred O_2 locations showed that, except for Oxy2, all O_2 positions in the MBH were connected by the tunnel network, which was also predicted by CAVER 3.0 (Fig. 2). In addition, Oxy5 and Oxy6, located close to the proposed tunnel entries, showed the highest transition probabilities (28.6% and 23.2%, respectively) to the "bulk region" (solvent and undefined regions within the protein), making these positions potential entry sites for O_2 (Fig. 3*B* and Table 4). The probability for a transition from the bulk region to branch 1 (Oxy1 and Oxy7) was much lower compared with transitions from the bulk region to positions Oxy5 and Oxy6 at the potential entry points (Table 4). Deeply buried sites, such as Oxy3 and the branch 1 region, showed higher self-transition probabilities (Table 4) and occupancies (Fig. 3*B*) than regions close to the protein surface (Oxy5 and Oxy6), indicating longer residence times for O_2 at these sites. The only difference between MD and CAVER 3.0 predictions was that in the MD simulations, the observed O_2 densities in tunnel A were lower than in tunnel B (Fig. 3), while CAVER 3.0 predicted tunnel A

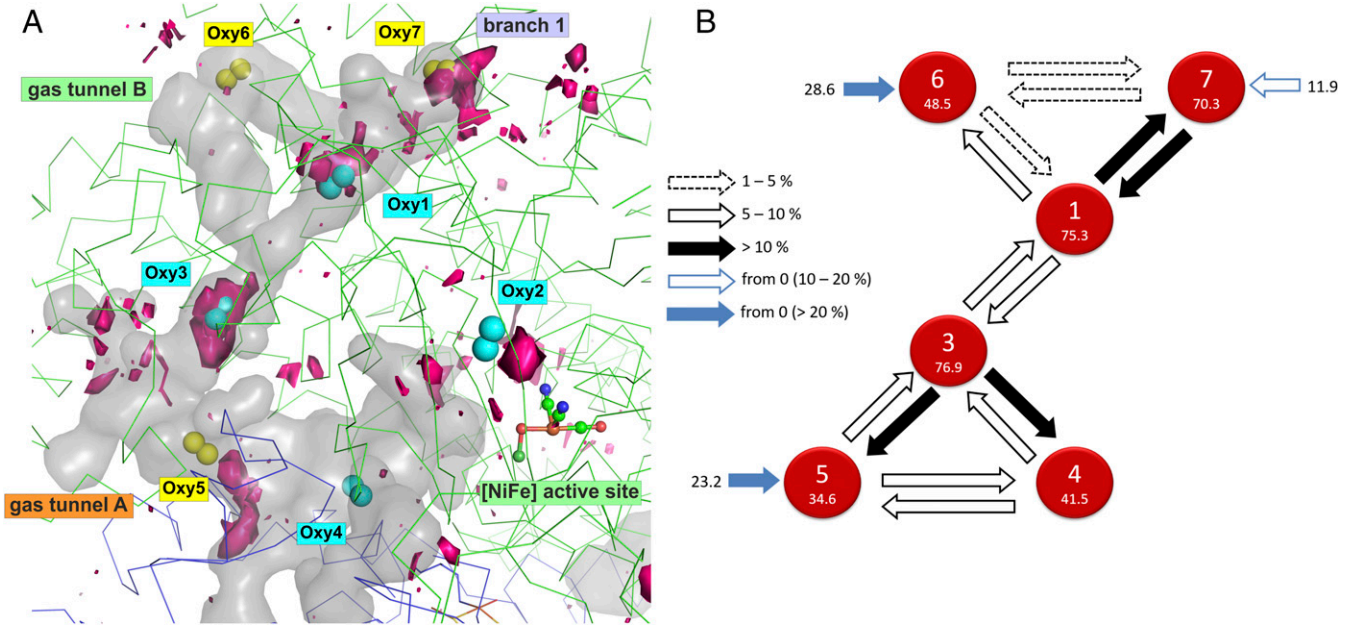

Fig. 3. Comparison of the experimentally determined O_2 positions in the predicted gas tunnels with the O_2 probability densities derived from MD simulations. (*A*) O_2 probability densities obtained from MD simulations (pink surface) are superimposed on the structure of O_2-derivatized MBH. The MBH tunnels calculated in PyMOL (29) are shown as a gray surface consisting of tunnel A, tunnel B, and branch 1. O_2 positions determined by the soak-and-freeze approach (24) are indicated as cyan and yellow spheres. The O_2 molecules 5–7 are shown only here, as they are not modeled in the actual MBH structure (PDB ID code 5MDL) due to their low occupancy. The backbone of the MBH is drawn in C-alpha representation, and the active site is drawn as a ball/stick model. (*B*) Calculated transition network consists of six sites (nodes) illustrated as red circles. The percental occupancy of each site is indicated within the circles. Transitions between nodes are highlighted as arrows, weighted according to their probabilities. Blue arrows mark regions with the highest transition probability coming from the bulk region "state 0" (as a percentage).

Table 4. Transition matrix for O_2 diffusion

State	Bulk	Oxy1	Oxy 2	Oxy 3	Oxy 4	Oxy 5	Oxy 6	Oxy 7
Bulk	99.6	0.0	0.0	0.0	0.0	0.0	0.0	0.0
Oxy 1	4.2	70.9	0.0	7.2	0.0	0.0	2.9	14.8
Oxy 2	11.0	0.0	88.9	0.0	0.0	0.0	0.0	0.0
Oxy 3	9.7	6.8	0.0	71.0	7.0	5.5	0.0	0.0
Oxy 4	9.2	0.0	0.0	14.3	69.4	7.1	0.0	0.0
Oxy 5	23.2	0.0	0.1	15.6	9.3	51.8	0.0	0.0
Oxy 6	28.6	5.1	0.0	0.0	0.0	0.0	62.9	3.4
Oxy 7	11.9	15.9	0.0	0.0	0.0	0.0	2.2	70.0

All directional (column to row) gas hopping probabilities are given as a percentage. The bulk region contains positions in the solvent or undefined areas in the protein.

as the main access pathway (Fig. 1). This finding may result from the increased flexibility of the amino acid side chains narrowing tunnel A in the simulations.

The spatial probability density of H_2 in the gas tunnel network was similar to that predicted for O_2 (Fig. S6). However, distinct differences in the diffusion properties of H_2 and O_2 were encountered. For the H_2 diffusion, tunnel A was strongly favored over tunnel B, as reflected by (*i*) the high transition probabilities between Oxy5 and Oxy4 (Table S1) and (*ii*) the increased occupancies of these sites (Fig. S6). Concomitantly, the low occupancy of Oxy3 (45.7% vs. 76.9% for H_2 and O_2, respectively) reflects a reduced diffusion of H_2 through tunnel B. Because of the smaller size and lower molecular weight of H_2 compared with O_2, higher H_2 densities were found in close vicinity (2.7-Å distance) to the [NiFe] center, as well as outside the MBH tunnel system in the protein matrix (Fig. S5).

To investigate whether the pressure treatment, which comes along with the soak-and-freeze method, had an impact on the overall structure of MBH and its gas tunnels, we compared the O_2-derivatized structure and a structure obtained after high-pressure (2,000 bar of helium) treatment of MBH crystals with the nonderivatized reference structure of MBH at ambient pressure (28). The crystal structures were aligned using the program PyMOL (29), and we obtained root mean square deviations (rmsds) of 0.043 Å and 0.195 Å when comparing the O_2-derivatized structure and the high-pressure structure with the reference MBH structure, respectively (Fig. S7). The greater differences with the high-pressure structure are also reflected by the B-factors (temperature factors). The B-factor comparison between the three structures was visualized using PyMOL in a range between 10 $Å^2$ and 50 $Å^2$ (Fig. 4). All O_2-derivatized MBH structures revealed no significant changes in the overall temperature factors upon pressurization compared with the REF datasets. Nevertheless, a further increase of the pressure to 2,000 bar led to a marked rise in the B-factors. The pressure-induced higher flexibility of amino acids even led to an unresolved disordered loop structure close to the entrance of tunnel A and in an enlargement of the surrounding area (Fig. 4). Furthermore, branch 1 of the hydrophobic tunnel is capped by a surface-located α-helix, which does not show an increase in flexibility through pressurization either at 70 bar or 2,000 bar. This supports the proposal of branch 1 being mainly a dead end and not a transient gas tunnel with a lockable lid. Notably, the [NiFe] active site, as well as the medial [3Fe4S] cluster and the distal [4Fe4S] cluster of the electron relay, maintained their spatial structure upon pressurization. In all three MBH structures,

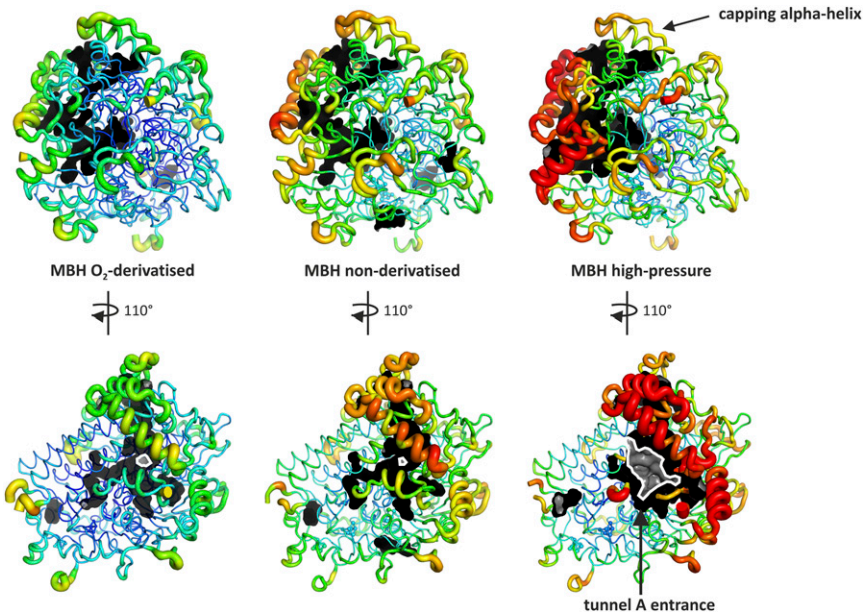

Fig. 4. Comparison of O_2-derivatized, nonderivatized, and high-pressure MBH structures on the basis of the B (temperature)-factors. All structures are shown in tube representation. Low to high B-factors are set to values from 10 to 50 $Å^2$ and represented in the PyMOL color-bar rainbow ranging from dark blue to red. The tube radius is scaled based on the B-factors. The hydrophobic tunnel is illustrated as a black surface with PyMOL (29). The lower structures are rotated by 110° and provide a view of the entry of tunnel A edged by a white line.

the Ni and Fe atoms have distances of 2.9 Å (Table 5), and they are bridged by a hydroxide ligand, which is entirely in line with the oxidation state of the catalytic center (18, 19). They also showed the typical open conformation of the proximal [4Fe3S] cluster with a bond length of ∼2.1 Å between iron 4 and the backbone nitrogen of cysteine 20 (Fig. S8), which is compatible with the as-isolated, superoxidized state of the enzyme (19). Despite the structural conformity, the [4Fe3S] cluster of the O_2-derivatized MBH showed two additional structural features compared with the reference structure. First, the carboxylate functional group of $E76_S$ is shifted toward Fe4 of the cluster (Fig. 5*A*), and, second, Fe1 carries a hydroxyl ligand (Fig. 5*B*). While the distance of $E76_S$ and Fe4 amounted to 3.4 Å and 3.2 Å in the reference and high-pressure structure, respectively, it was reduced to 2.6 Å in the O_2-derivatized MBH (Fig. 5*A* and Tables 2 and 5). The $E76_S$ shift toward the proximal cluster was observed in all of the O_2-derivatized MBH structures (Tables 1 and 2). In the as-isolated structure of the membrane-bound O_2-tolerant [NiFe] hydrogenase 1 from *Escherichia coli* (*Ec*Hyd-1), the $E76_S$ was found in a double conformation with distances of 4.9 Å and 2.4 Å of the glutamate-derived carboxylate O_ε to Fe4 (30). Volbeda et al. (30) proposed that $E76_S$ functions as a base for deprotonation of the carboxamido N of cysteine 20, which further enables the Fe4 to bind to the backbone of cysteine 20, and thus stabilizes the high-potential form of the [4Fe3S] cluster. A similar cluster stabilization was proposed for the Fe1-bound hydroxyl ligand in MBH. The presence of this ligand with an Fe-O distance of 1.8 Å between the hydroxyl oxygen and the Fe1 was confirmed in all of the O_2-derivatized MBH structures. The hydroxyl ligand has an average occupancy of ∼34%, with no obvious relation to the O_2 concentration (Table 1). In the REF datasets, however, the Fe1-bound hydroxyl ligand was not visible. In the previously published crystal structures of as-isolated, superoxidized MBH, the hydroxyl ligand occurred with high variation in occupancy, reaching from 0% in PDB ID code 4TTT, to 30% in PDB ID code 4IUC (B-factor: 9 $Å^2$), and up to 88% in PDB ID code 4IUB (B-factor: 11 $Å^2$) (19). At present, it remains unclear whether the Fe1-bound hydroxyl ligand and the $E76_S$ shift are related to the 5+/4+ redox state transition of the [4Fe3S] cluster (19) or represent damage caused by high O_2 concentrations. Nevertheless, it is important to note that no remarkable damage due to high O_2 pressure and/or radiation was observed for the remaining metal cofactors in the MBH. Moreover, the two structural features might point to a dedicated function. In the course of MBH preparation, the enzyme was oxidized by ferricyanide and air. However, the occurrence of the OH^- ligand varied significantly (0–88%) in these preparations (19). Upon derivatization under pressurized pure O_2, the redox potential was presumably further raised, which is why we are able to see stable occupancies of the OH^- ligand and the $E76_S$ shift in all corresponding MBH structures. This also leads to the question of whether the hydroxyl ligand at Fe1 of the proximal [4Fe3S] cluster arises from surrounding water molecules or from molecular oxygen. Previous resonance Raman experiments using $^{18}O_2$ labeling showed an isotopic shift for the

Table 5. Selected interatomic distances at the [NiFe] site and the [4Fe3S] cluster

Interatomic distance	O_2-derivatized	High pressure	Reference
[NiFe] active site Ni-Fe distance, Å	2.9	2.9	2.9
[4Fe3S] cluster Fe4-N20 distance, Å	2.1	2.2	2.2
[4Fe3S] cluster Fe4-$E76_S$ distance, Å	2.6	3.2	3.4

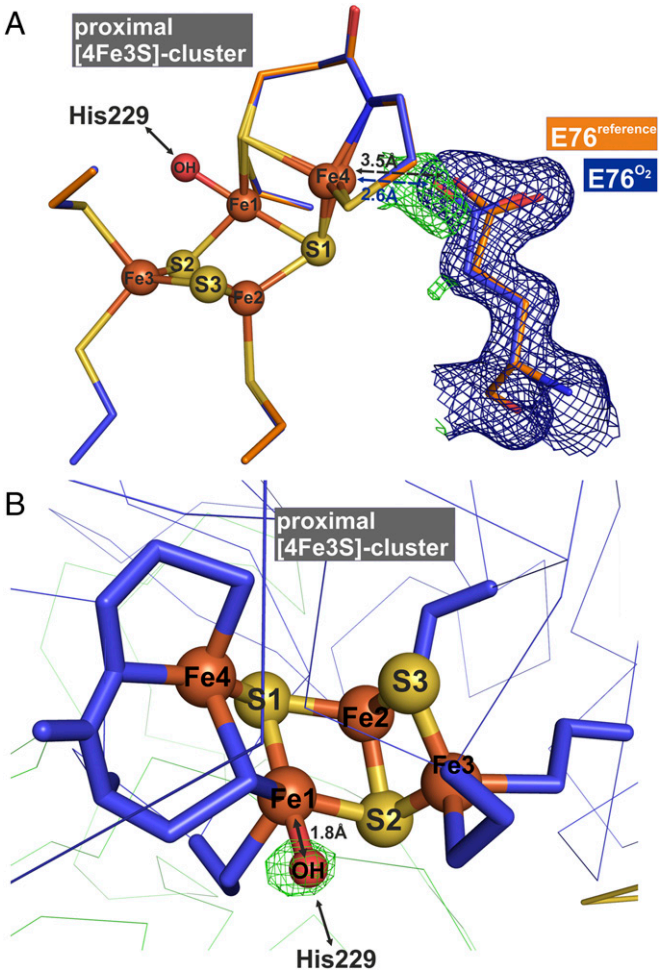

Fig. 5. Proximal [4Fe3S] cluster of O_2-derivatized MBH. (*A*) [4Fe3S] cluster of O_2-derivatized (PDB ID code 5MDL, blue) and nonderivatized (PDB entry 5MDK, orange) MBH is shown in ball/stick representation in its as-isolated state with an open conformation. The 2m*Fo* − D*Fc* electron density map of $E76^{reference}$ is illustrated as blue mesh and contoured at 1σ. The $Fo^{O_2} - Fo^{reference}$ electron density map is depicted as green mesh and contoured at 3σ. (*B*) Proximal cluster is shown in its superoxidized (as-isolated) state with an open conformation and the hydroxyl ligand bound to Fe1 with a distance of 1.8 Å. The positive m*Fo* − D*Fc* electron density map of the hydroxyl ligand is illustrated as green mesh and contoured at 3σ.

Fe-OH stretching mode, leading to the conclusion of an O_2-derived ligand (19). Therefore, the additional ligand at Fe1 of the [4Fe3S] cluster could be part of an O_2-reducing mechanism, where His229, which is in hydrogen-bonding distance to the hydroxyl ligand, might play an important role in delivering protons produced in the H_2 oxidation reaction at the active site. A recent publication by Dance (31) describes a theoretical model of the communication between the catalytic center and the proximal cluster via conformational changes of residues terminating in this highly conserved His229. This histidine plays a crucial role in transmitting a proton to the opposite side of the proximal cluster for protonation of sulfur S3, followed by an opening of the Fe4-S3 bond. It has been stated that a close water molecule (4.5 Å away from Fe1) could be involved in an OH_2/OH^- turnover to provide the H^+ for the separate proximal cluster proton cycle. This result is consistent with our structural findings for the proximal cluster in O_2-derivatized MBH. S3 protonation, however, does not lead to the Fe4-N20 bond according to Dance (31). Here, a second protonation/deprotonation cycle is

necessary, which might be facilitated by Glu76. In our structural data, we can confirm an interaction of Glu76 with the proximal cluster under aerobic, oxygen-derivatized conditions. However, a sequence of protonation or different intermediates cannot be assigned in our structures and requires further experiments. It needs to be elucidated whether the OH^- ligand could also originate from the surrounding water network. In this case, the proton released from water dissociation might be transferred via His229 (Fig. 5) to the catalytic center to support O_2 reduction to water. Additionally, the OH^- ligand may stabilize the superoxidized state of the proximal cluster (19).

In summary, the technique of crystal derivatization (soak-and-freeze) enables unprecedented insight into the accessibility of the MBH tunnel network for gas molecules. Our data show that MBH contains several hydrophobic tunnels that can be traced via several O_2 molecules residing at defined sites. MD simulations further manifest the pathways used by the gas molecules traveling from the protein surface to the deeply buried active site. Furthermore, the MD simulations indicate that O_2 and the much smaller H_2 molecules likely use the same routes within the gas tunnel network. Additional gas diffusion studies might provide supplementary information on the migration behavior of H_2 and O_2 within the MBH gas tunnel network under ambient conditions. For example, a previous experimental study on [FeFe] hydrogenases revealed that high H_2 levels decreased the inhibition by O_2 (32). Our MD simulations already revealed differences in the distribution of O_2 and H_2. O_2 occupies the two transition sites of tunnel A to a much lesser extent than H_2 does. O_2 might be primarily directed toward branch 1 of gas tunnel B, which is located far away from the vulnerable [NiFe] active site. This indicates a mechanism that, at least to some degree, can separate the two gases H_2 and O_2 from each other, and would thus be another adaptation of O_2-tolerant hydrogenases toward prevention of damage by molecular oxygen. However, our data do not exclude accessibility of O_2 to the [NiFe] active site. Understanding the architecture of the tunnel network in MBH is crucial for future modifications of the enzyme functions through engineering of the tunnel characteristics. Site-directed amino acid exchanges allow changing the physical tunnel properties, such as the diameter and hydrophobicity. These modifications may have an influence on both the access of the substrate H_2 to the active site and the susceptibility of the enzyme toward O_2.

Materials and Methods

Protein Expression and Purification. Native MBH was produced and purified in the as-isolated (air-oxidized) state as described elsewhere (18, 33).

Crystallization. MBH was crystallized with the sitting-drop vapor diffusion method in 24-well Linbro plates (Jena Bioscience) at a concentration of about 10 $mg{\cdot}mL^{-1}$ and at 277 K. The reservoir solution contained 20–30% polyethylene glycol 3350 and 100 mM Bis-(2-hydroxy-ethyl)-amino-Tris(hydroxylmethyl)-methane buffer at pH 5.5–6.5. Precipitants and protein solution were mixed in different ratios (7–8 μL) into microbridges (Hampton Research). After 2–4 d, the dark-brown, needle-shaped MBH crystals were directly used for high-pressure cooling and O_2 derivatization experiments or were cryoprotected in 15% glycerol and flash-cooled in LN2 as reference data collection.

High-Pressure Cryocooling. The cryoprotectant free cooling of the MBH crystals was performed using a high-pressure cooling system recently developed at the ESRF (28). The needle-shaped crystals were directly harvested from the crystallization drop with specific pluggable sample supports (MiTeGen) and transferred into the pressurizing drop tubes at room temperature. The lower parts of the drop tubes were then cooled in LN2, and the crystals were pressurized with 2,000 bar of helium. Thereafter, the crystals were dropped into the bottom of the tube and flash-cooled at 77 K. Finally, the system was depressurized, and the crystals were handled in LN2 and stored under LN2 for further X-ray experiments. Four crystals were high-pressure-cooled at the same time.

O_2 Derivatization. The MBH crystals were derivatized with O_2 gas in a cryogenic oxygen pressure cell newly developed at the ESRF (24). Each time, one crystal was harvested from the crystallization drop with a specific pluggable sample support (MiTeGen) being surrounded by mother liquor, including 15% glycerol. The crystal was then loaded into the pressurizing drop tube at room temperature. The MBH crystals were pressurized at 56 bar (5,600 kPa) and 70 bar (7,000 kPa) in a time frame from 15 to 70 min. Still under pressure, the crystal was dropped into the bottom of the tube and flash-cooled in liquid O_2 at 77 K. After depressurizing the system, the crystal was handled in LN2 with a specially designed cryotoolkit and stored in LN2 for further X-ray experiments.

Structure Analysis. Diffraction data were collected at the ESRF. The best high-pressure (HP) dataset was collected at the tunable beamline ID29 (34) with a PILATUS 6M-F detector at a wavelength of 0.976 Å. The best OxD and REF datasets were collected at the tunable beamline ID30B (35) with a PILATUS 6M-F detector at a wavelength of 0.976 Å. All datasets were measured using data collection and the strategy software packages MxCube (36) and EDNA (37). The data collection was carried out in the helical rotation mode at 100 K; a rotation increment of 0.05° with an exposure time of 0.037 s for each frame (3,000 images collected); and detector-to-crystal distances of 191 mm, 163 mm, and 256 mm for the HP, OxD, and REF datasets, respectively. The images of the best dataset were indexed, integrated, and scaled using the XDS program package (38) and the CCP4 (39) program SCALA (40) All crystals showed an orthorhombic space group $P2_12_12_1$ (unit cell constants HP dataset: a = 73.39 Å, b = 95.70 Å, c = 121.57 Å and $\alpha = \beta = \gamma = 90.00°$; unit cell constants OxD dataset: a = 73.13 Å, b = 95.57 Å, c = 119.69 Å and $\alpha = \beta = \gamma = 90.00°$, unit cell constants REF dataset: a = 73.11 Å, b = 95.57 Å, c = 119.83 Å and $\alpha = \beta = \gamma = 90.00°$). Initial phases for MBH (HP, OxD, and REF datasets) were obtained by molecular replacement based on the crystal structure of the as-isolated MBH (PDB ID code 4TTT) as the initial search model using the CCP4 program PHASER (41, 42). Subsequently, different refinement strategies (*inter alia* real-space refinement and B-factor refinements) and simulated annealing (slow cooling protocol, maximum likelihood target function, and energy minimization) were carried out. We used additional simulated annealing as an optimization method performed with the PHENIX suite to remove model bias and displayed the results as "simulated annealing composite omit" maps (43) (Fig. S1 *M–P*). The search for water molecules was performed with the PHENIX suite (43). The crystal structure was finalized with the CCP4 program REFMAC5 (44). Manual rebuilding of HP, OxD, and REF dataset models and electron density interpretation were performed after each refinement cycle using the program Coot (45). The final OxD model has agreement factors R_{free}/R_{work} of 13.2%/16.3% (46). Structure validations were performed with the programs of the Research Collaboratory for Structural Bioinformatics PDB Validation server (47), MolProbity server (48) and WHAT IF server (49). All molecular graphics representations were created using PyMOL (29). Table 6 summarizes the statistics for crystallographic data collection and structural refinement.

CAVER Tunnel Calculation. The program CAVER 3.0 was used as a PyMOL plug-in (25, 29). The settings in the program were manually adjusted. The initial starting point [NH_2 of the guanidine group of the arginine (i.e., $R530_L$ for MBH)], shell depth (2 Å), shell radius (3 Å), cluster threshold (3.5 Å), desired radius (5 Å), and maximum distance (3 Å) were maintained constant for all calculations. The maximum distance specifies the furthest point (from the initial arginine) to start a tunnel calculation. The bottleneck radius is the narrowest part of a given tunnel and corresponds to the minimum probe radius. The tunnel analysis provides a list of calculated tunnels (residues) with their bottleneck residues, which were used to draw Fig. S1. The tunnels are ranked according to a specific cost function (e.g., for two tunnels with equal radii, the one with the shorter distances has a lower cost) (25). The tunnel with the lowest cost is the primary tunnel.

MD Simulations. Classical MD simulations were performed to investigate the diffusion of O_2 and H_2 within MBH. For this, the coordinates of reduced MBH (PDB ID code 3RGW) were used as the starting configuration (18). While the protein was described with the Gromos53a6 united force field (50), the inorganic ligands ([NiFe] active site and [FeS] clusters) were treated as rigid bodies using the LINCS algorithm (51). Their partial charges were adopted from an earlier work (52). The protein-cofactor model was solvated in a cubic preequilibrated single point charge (SPC) model water box (53) under *ca.* 25 mM NaCl. Additionally, O_2 (or H_2) molecules mimicking a concentration of *ca.* 225 mM were inserted randomly, replacing bulk water molecules. The high concentration of oxygen was used to increase the interaction with MBH similar how it was done for the standard hydrogenase (23). Both gas molecules were simulated as a three-site model as described in literature (23).

After stepwise energy minimization and thermal equilibration at 300 K, the system was subjected to a 300-ns-long production run. During the simulation

Table 6. Data collection and refinement statistics

	MBH (PDB ID code)		
PDB ID code	O_2-derivatized (5MDL)	High pressure (5MDJ)	Nonderivatized (as-isolated) (5MDK)
Data collection	ESRF, ID30B	ESRF, ID29	ESRF, ID30B
Space group	$P2_12_12_1$	$P2_12_12_1$	$P2_12_12_1$
Cell dimensions			
a, b, c, Å	73.13, 95.57, 119.69	73.39, 95.70, 121.57	73.11, 95.57, 119.83
α, β, γ; °	90, 90, 90*	90, 90, 90*	90, 90, 90*
Resolution, Å	47.78–1.41 (1.49–1.41)†	47.85–1.48 (1.56–1.48)†	47.78–1.50 (1.58–1.50)†
R_{merge} (58)	0.064 (0.681)†	0.064 (0.839)†	0.060 (0.800)†
I/(σ)I (59)	10.7 (2.0)†	12.5 (2.0)†	12.4 (1.9)†
CC1/2‡	100 (89.6)†	100 (82.6)†	100 (88)†
Completeness, %	96.4 (94.4)†	99.8 (99.4)†	99.8 (98.9)†
Redundancy	4.8 (4.6)†	5.6 (5.2)†	5.4 (5.2)†
Wilson B-factor, $Å^2$	14.4	20.7	19.9
Refinement			
Resolution, Å	1.41	1.48	1.50
No. of reflections	147,390	135,294	127,184
R_{work}/R_{free}, %	13.2/16.3	14.2/17.2	12.5/15.3
No. of atoms/residues			
Large subunit (HoxG)	4,774/601	4,687/601	4,776/601
Small subunit (HoxK)	2,118/269	2,051/268	2,142/269
Others			
[FeS] clusters	22/3	22/3	22/3
[NiFe] active site	9/1	9/1	9/1
Water	611/603	471/466	653/652
Dioxygen	8/4	0	0
Cl^-	1/1	1/1	5/3
Mg^{2+}	1/1	1/1	1/1
Polyethylene glycol	7/1	0	0
Mean B-factor (all atoms), $Å^2$	19.6	27.5	25.7
rmsd			
Bond lengths, Å	0.008	0.010	0.007
Bond angles, °	1.260	1.357	1.302
Ramachandran plot,§ (60)			
Most favored, %	98	98	98
Allowed/disallowed	2/0	2/0	2/0

*One crystal was used.
†Highest resolution shell is shown in parentheses.
‡Half-set correlation coefficient.
§As defined in the program RAMPAGE.

carried out with Gromacs 4.6.5 (54), a time step of 2 fs was enabled by constraining all bonds containing hydrogen atoms by the LINCS algorithm (51). The NPT ensemble [constant number of particles, pressure (P = 1 atm) and temperature (T = 300 K)] under periodic boundary conditions was realized by the Berendsen pressure (55) and v-rescale temperature (56) methods, applying pressure and temperature coupling constants of τ_p = 1.0 ps and τ_T = 0.1 ps, respectively. Electrostatic interactions beyond a cutoff of 1.4 nm were modeled by the particle mesh Ewald summation (57), and van der Waals interactions were truncated beyond 1.2 nm.

Gas Transition Models. The diffusion of O_2 and H_2 within the MBH was described by a simple transition model based on the O_2 (H_2) dynamics extracted from the MD simulations. In total, eight regions were defined. Seven regions correspond to spheres of 5 Å around the amino acids surrounding oxygen molecules (Oxy1–7) in the crystal structure. Bulk solvent (or region 0) contained all gas molecules outside these six defined spheres (solvent and undefined positions in MBH). Based on this model, transitions between these regions were analyzed for all O_2 (H_2) molecules using a time resolution of 20 ps. Furthermore, occupancies were calculated taking the last 150 ns of the trajectory into account.

ACKNOWLEDGMENTS. We thank Uwe Müller, Manfred Weiss, and the scientific staff of the BESSY-MX (Macromolecular X-ray Crystallography)/Helmholtz Zentrum Berlin für Materialien und Energie at beamlines BL14.1, BL14.2, and BL14.3 operated by the Joint Berlin MX-Laboratory at the BESSY II electron storage ring (Berlin-Adlershof, Germany) as well as the scientific staff of the ESRF (Grenoble) at beamlines ID30A-3, ID30B, ID23-1, ID23-2, and ID29, where the data were collected, for continuous support. We also thank the "Norddeutscher Verbund für Hoch-und Höchstleistungsrechnen" for providing HPC resources. This work was supported by grants from the ESRF (to G.G., D.v.S., P.v.d.L., A.R., and P.C.), Deutsche Forschungsgemeinschaft (DFG; Grants SFB740-B6 and SFB1078-B6 to P.S.), and DFG Cluster of Excellence "Unifying Concepts in Catalysis" (Research Field D3/E3-1 to J.K., A.S., S.F., T.U., M.A.M., O.L., and P.S.).

1. Raushel FM, Thoden JB, Holden HM (2003) Enzymes with molecular tunnels. *Acc Chem Res* 36:539–548.
2. Huang X, Holden HM, Raushel FM (2001) Channeling of substrates and intermediates in enzyme-catalyzed reactions. *Annu Rev Biochem* 70:149–180.
3. Thoden JB, Holden HM, Wesenberg G, Raushel FM, Rayment I (1997) Structure of carbamoyl phosphate synthetase: A journey of 96 A from substrate to product. *Biochemistry* 36:6305–6316.
4. Krahn JM, et al. (1997) Coupled formation of an amidotransferase interdomain ammonia channel and a phosphoribosyltransferase active site. *Biochemistry* 36:11061–11068.
5. van den Heuvel RHH, et al. (2002) Structural studies on the synchronization of catalytic centers in glutamate synthase. *J Biol Chem* 277:24579–24583.
6. Mouilleron S, Badet-Denisot MA, Golinelli-Pimpaneau B (2006) Glutamine binding opens the ammonia channel and activates glucosamine-6P synthase. *J Biol Chem* 281: 4404–4412.

7. Klvana M, et al. (2009) Pathways and mechanisms for product release in the engineered haloalkane dehalogenases explored using classical and random acceleration molecular dynamics simulations. *J Mol Biol* 392:1339–1356.
8. Coulombe R, Yue KQ, Ghisla S, Vrielink A (2001) Oxygen access to the active site of cholesterol oxidase through a narrow channel is gated by an Arg-Glu pair. *J Biol Chem* 276:30435–30441.
9. Banthiya S, et al. (2016) Structural and functional basis of phospholipid oxygenase activity of bacterial lipoxygenase from Pseudomonas aeruginosa. *Biochim Biophys Acta* 1861:1681–1692.
10. Kalms J, et al. (2017) The crystal structure of Pseudomonas aeruginosa lipoxygenase Ala420Gly mutant explains the improved oxygen affinity and the altered reaction specificity. *Biochim Biophys Acta* 1862:463–473.
11. Leroux F, et al. (2008) Experimental approaches to kinetics of gas diffusion in hydrogenase. *Proc Natl Acad Sci USA* 105:11188–11193.
12. Wagner T, Ermler U, Shima S (2016) The methanogenic CO2 reducing-and-fixing enzyme is bifunctional and contains 46 [4Fe-4S] clusters. *Science* 354:114–117.
13. Kalms J, et al. (2016) Krypton derivatization of an O2-tolerant membrane-bound [NiFe] hydrogenase reveals a hydrophobic tunnel network for gas transport. *Angew Chem Int Ed Engl* 55:5586–5590.
14. Kubas A, et al. (2017) Mechanism of O2 diffusion and reduction in FeFe hydrogenases. *Nat Chem* 9:88–95.
15. Liebgott PP, et al. (2010) Relating diffusion along the substrate tunnel and oxygen sensitivity in hydrogenase. *Nat Chem Biol* 6:63–70.
16. Duché O, Elsen S, Cournac L, Colbeau A (2005) Enlarging the gas access channel to the active site renders the regulatory hydrogenase HupUV of Rhodobacter capsulatus O2 sensitive without affecting its transductory activity. *FEBS J* 272:3899–3908.
17. Buhrke T, Lenz O, Krauss N, Friedrich B (2005) Oxygen tolerance of the H2-sensing [NiFe] hydrogenase from Ralstonia eutropha H16 is based on limited access of oxygen to the active site. *J Biol Chem* 280:23791–23796.
18. Fritsch J, et al. (2011) The crystal structure of an oxygen-tolerant hydrogenase uncovers a novel iron-sulphur centre. *Nature* 479:249–252.
19. Frielingsdorf S, et al. (2014) Reversible [4Fe-3S] cluster morphing in an O(2)-tolerant [NiFe] hydrogenase. *Nat Chem Biol* 10:378–385.
20. Fritsch J, Lenz O, Friedrich B (2013) Structure, function and biosynthesis of O_2-tolerant hydrogenases. *Nat Rev Microbiol* 11:106–114.
21. Wulff P, Day CC, Sargent F, Armstrong FA (2014) How oxygen reacts with oxygen-tolerant respiratory [NiFe]-hydrogenases. *Proc Natl Acad Sci USA* 111:6606–6611.
22. Cohen J, Kim K, King P, Seibert M, Schulten K (2005) Finding gas diffusion pathways in proteins: Application to O2 and H2 transport in CpI [FeFe]-hydrogenase and the role of packing defects. *Structure* 13:1321–1329.
23. Wang P, Best RB, Blumberger J (2011) Multiscale simulation reveals multiple pathways for H2 and O2 transport in a [NiFe]-hydrogenase. *J Am Chem Soc* 133:3548–3556.
24. Lafumat B, et al. (2016) Gas-sensitive biological crystals processed in pressurized oxygen and krypton atmospheres: Deciphering gas channels in proteins using a novel 'soak-and-freeze' methodology. *J Appl Crystallogr* 49:1478–1487.
25. Chovancova E, et al. (2012) CAVER 3.0: A tool for the analysis of transport pathways in dynamic protein structures. *PLoS Comput Biol* 8:e1002708.
26. Montet Y, et al. (1997) Gas access to the active site of Ni-Fe hydrogenases probed by X-ray crystallography and molecular dynamics. *Nat Struct Biol* 4:523–526.
27. Baltazar CSA, Teixeira VH, Soares CM (2012) Structural features of [NiFeSe] and [NiFe] hydrogenases determining their different properties: A computational approach. *J Biol Inorg Chem* 17:543–555.
28. Van Der Linden P, et al. (2014) Towards a high-throughput system for high-pressure cooling of cryoprotectant-free biological crystals. *J Appl Crystallogr* 47:584–592.
29. Delano WL (2002) The PyMOL molecular graphics system (Schrödinger LLC, San Carlos, CA), Version 0.99rc6.
30. Volbeda A, et al. (2012) X-ray crystallographic and computational studies of the O2-tolerant [NiFe]-hydrogenase 1 from Escherichia coli. *Proc Natl Acad Sci USA* 109: 5305–5310.
31. Dance I (2015) What is the trigger mechanism for the reversal of electron flow in oxygen-tolerant [NiFe] hydrogenases? *Chem Sci* 6:1433–1443.
32. Stripp ST, et al. (2009) How oxygen attacks [FeFe] hydrogenases from photosynthetic organisms. *Proc Natl Acad Sci USA* 106:17331–17336.
33. Goris T, et al. (2011) A unique iron-sulfur cluster is crucial for oxygen tolerance of a [NiFe]-hydrogenase. *Nat Chem Biol* 7:310–318.
34. de Sanctis D, et al. (2012) ID29: A high-intensity highly automated ESRF beamline for macromolecular crystallography experiments exploiting anomalous scattering. *J Synchrotron Radiat* 19:455–461.
35. Theveneau P, et al. (2013) The upgrade programme for the structural biology beamlines at the European Synchrotron Radiation Facility-high throughput sample evaluation and automation. *J Phys Conf Ser* 425:8–12.
36. Gabadinho J, et al. (2010) MxCuBE: A synchrotron beamline control environment customized for macromolecular crystallography experiments. *J Synchrotron Radiat* 17:700–707.
37. Incardona MF, et al. (2009) EDNA: A framework for plugin-based applications applied to X-ray experiment online data analysis. *J Synchrotron Radiat* 16:872–879.
38. Kabsch W (2010) XDS. *Acta Crystallogr D Biol Crystallogr* 66:125–132.
39. Collaborative Computational Project, Number 4 (1994) The CCP4 suite: Programs for protein crystallography. *Acta Crystallogr D Biol Crystallogr* 50:760–763.
40. Evans P (2006) Scaling and assessment of data quality. *Acta Crystallogr D Biol Crystallogr* 62:72–82.
41. Winn MD, et al. (2011) Overview of the CCP4 suite and current developments. *Acta Crystallogr D Biol Crystallogr* 67:235–242.
42. McCoy AJ, et al. (2007) Phaser crystallographic software. *J Appl Crystallogr* 40: 658–674.
43. Adams PD, et al. (2010) PHENIX: A comprehensive Python-based system for macromolecular structure solution. *Acta Crystallogr D Biol Crystallogr* 66:213–221.
44. Murshudov GN, Vagin AA, Dodson EJ (1997) Refinement of macromolecular structures by the maximum-likelihood method. *Acta Crystallogr D Biol Crystallogr* 53: 240–255.
45. Emsley P, Lohkamp B, Scott WG, Cowtan K (2010) Features and development of Coot. *Acta Crystallogr D Biol Crystallogr* 66:486–501.
46. Brünger AT (1992) Free R value: A novel statistical quantity for assessing the accuracy of crystal structures. *Nature* 355:472–475.
47. Berman HM, et al. (2000) The Protein Data Bank. *Nucleic Acids Res* 28:235–242.
48. Davis IW, et al. (2007) MolProbity: All-atom contacts and structure validation for proteins and nucleic acids. *Nucleic Acids Res* 35:W375–W383.
49. Rodriguez R, Chinea G, Lopez N, Pons T, Vriend G (1998) Homology modeling, model and software evaluation: Three related resources. *Bioinformatics* 14:523–528.
50. Oostenbrink C, Soares TA, van der Vegt NFA, van Gunsteren WF (2005) Validation of the 53A6 GROMOS force field. *Eur Biophys J* 34:273–284.
51. Hess B, Bekker H, Berendsen HJC, Fraaije JGEM (1997) LINCS: A linear constraint solver for molecular simulations. *J Comput Chem* 18:1463–1472.
52. Rippers Y, Utesch T, Hildebrandt P, Zebger I, Mroginski MA (2011) Insights into the structure of the active site of the O2-tolerant membrane bound [NiFe] hydrogenase of R. eutropha H16 by molecular modelling. *Phys Chem Chem Phys* 13:16146–16149.
53. Berendsen HJC, Postma JPM, van Gunsteren WF, Hermans J (1981) Interaction models of water in relation to protein hydration. *Intermolecular Forces: Proceedings of the Fourteenth Jerusalem Symposium on Quantum Chemistry and Biochemistry*, ed Pullman B (D. Reidel Publishing Company, Dordrecht, The Netherlands), pp 331–342.
54. Van Der Spoel D, et al. (2005) GROMACS: Fast, flexible, and free. *J Comput Chem* 26: 1701–1718.
55. Berendsen HJC, Postma JPM, van Gunsteren WF, DiNola A, Haak JR (1984) Molecular dynamics with coupling to an external bath. *J Chem Phys* 81:3684–3690.
56. Bussi G, Donadio D, Parrinello M (2007) Canonical sampling through velocity rescaling. *J Chem Phys* 126:014101.
57. Darden T, York D, Pedersen L (1993) Particle mesh Ewald: An N·log(N) method for Ewald sums in large systems. *J Chem Phys* 98:10089–10092.
58. Weiss MS (2001) Global indicators of X-ray data quality. *J Appl Crystallogr* 34:130–135.
59. Einspahr HM, Weiss MS (2012) *International tables for crystallography*, eds Arnold E, Himmel DM, Rossmann MG (Wiley, Chichester, UK), 2nd Ed, Vol F, pp 64–74.
60. Lovell SC, et al. (2003) Structure validation by C alpha geometry: phi, psi and C beta deviation. *Proteins* 50:437–450.